

See discussions, stats, and author profiles for this publication at: <https://www.researchgate.net/publication/256075458>

Polymer Crystallization as a Tool To Pattern Hybrid Nanostructures: Growth of 12 nm ZnO Arrays in Poly(3-hexylthiophene)

ARTICLE *in* NANO LETTERS · AUGUST 2013

Impact Factor: 13.59 · DOI: 10.1021/nl4024275 · Source: PubMed

CITATIONS

9

READS

58

12 AUTHORS, INCLUDING:



Sven Huettner

University of Bayreuth

51 PUBLICATIONS 1,695 CITATIONS

SEE PROFILE



Caterina Ducati

University of Cambridge

176 PUBLICATIONS 6,365 CITATIONS

SEE PROFILE



Kevin P Musselman

University of Waterloo

38 PUBLICATIONS 572 CITATIONS

SEE PROFILE

Polymer Crystallization as a Tool To Pattern Hybrid Nanostructures: Growth of 12 nm ZnO Arrays in Poly(3-hexylthiophene)

Reza Saberi Moghaddam,[†] Sven Huettner,[†] Yana Vaynzof,[†] Caterina Ducati,[‡] Giorgio Divitini,[‡] Ruth H. Lohwasser,[§] Kevin P. Musselman,^{†,‡} Alessandro Sepe,[†] Maik R. J. Scherer,[†] Mukundan Thelakkat,[§] Ullrich Steiner,[†] and Richard H. Friend^{*,†}

[†]Cavendish Laboratory, University of Cambridge, JJ Thomson Avenue, Cambridge CB3 0HE, United Kingdom

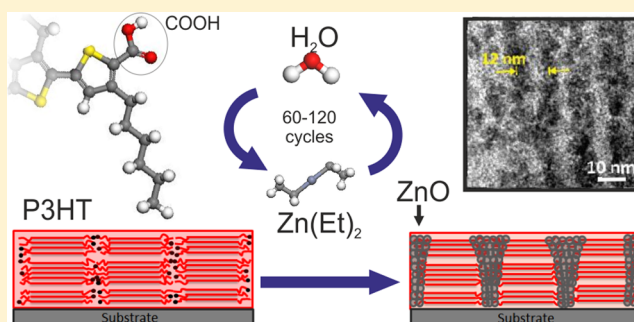
[‡]Department of Material Science and Metallurgy, University of Cambridge, Pembroke Street, Cambridge CB2 3QZ, United Kingdom

[§]Department of Macromolecular Chemistry I, University of Bayreuth, Universitätsstrasse 30, 95440, Bayreuth, Germany

Supporting Information

ABSTRACT: Well-ordered hybrid materials with a 10 nm length scale are highly desired. We make use of the natural length scale (typically 10–15 nm) of the alternating crystalline and amorphous layers that are generally found in semicrystalline polymers to direct the growth of a semiconducting metal oxide. This approach is exemplified with the growth of ZnO within a carboxylic acid end-functionalized poly(3-hexylthiophene) (P3HT–COOH). The metal-oxide precursor vapors diffuse into the amorphous parts of the semicrystalline polymer so that sheets of ZnO up to 0.5 μm in size can be grown. This P3HT–ZnO nanostructure further functions as a donor–acceptor photovoltaic system, with length scales appropriate for charge photogeneration.

KEYWORDS: Hybrid nanostructures, zinc oxide, poly(3-hexylthiophene), P3HT–ZnO, atomic layer deposition



Hybrid organic–inorganic nanostructures provide attractive routes to functional structures with applications in optoelectronics,^{1,2} biomedical sensors,^{3,4} and energy storage^{5,6} and conversion.^{7,8} The functionality of these structures is determined by the nanomorphology and the control of interfacial structures between the organic and the inorganic counterparts. ZnO is an interesting wide band gap semiconductor for use in these applications because of its low crystallization temperature.^{9,10} Difficulty in the control of crystal formation on the 10 nm length scale, however, has prevented the formation of the well-defined ZnO nanomorphologies required in hybrid electronic materials.

Here, we present a method in which the natural length scale of semicrystalline polymers directs the growth of a metal oxide to form a well-ordered hybrid structure on a 10 nm length scale. Isotactic polymer can crystallize into stacks of ~ 10 nm wide lamellae separated by similarly wide amorphous sheets which collect structural and morphological chain segments that cannot be incorporated into the crystalline domains (end groups, regioregular defects, chain-folds, entanglement points, Figure 1a). By introducing a functional end group to the polymer which accumulates within the amorphous interlayers, we can direct the incorporation of the metal oxide within the polymer nanostructure. Precursors can diffuse into the amorphous interlayers which enables the synthesis of ZnO within the semicrystalline P3HT in a strategy that is

reminiscent of atomic layer deposition (ALD). Rather than coating compact layers on top of a substrate or scaffold layer, we allow the precursors to diffuse into the amorphous bulk of the COOH-terminated P3HT. These functional end groups act as the initial reaction site for the metal oxide formation. Cycling the two precursor gases results in the build-up of several nanometer wide ZnO sheets, spanning the entire width of the aligned P3HT layer. The crystalline domains retain their integrity and functionality so that the polymer can act as an active component in addition to its role in directing the 3D growth of ZnO.

This approach contrasts the many conventional fabrication strategies for hybrid photovoltaic devices which include: (a) solution-processing of metal-oxide nanoparticles and a polymer to form the donor–acceptor blend,^{11,12} (b) backfilling of a mesoporous or nanostructured metal oxide scaffold with a polymer,^{13,14} and (c) the reaction of chemical precursors to form the metal oxide within the polymer film.^{15–17} Nanoparticle blends give convenient band gap tunability; however they offer little control of the nanomorphology since they rely on the agglomeration of nanoparticles. Charge transport is limited by the discontinuity of the nanoparticle domains and might be further hindered by the presence of ligands. These issues are avoided in prestructured inorganic scaffolds as they

Published: August 21, 2013

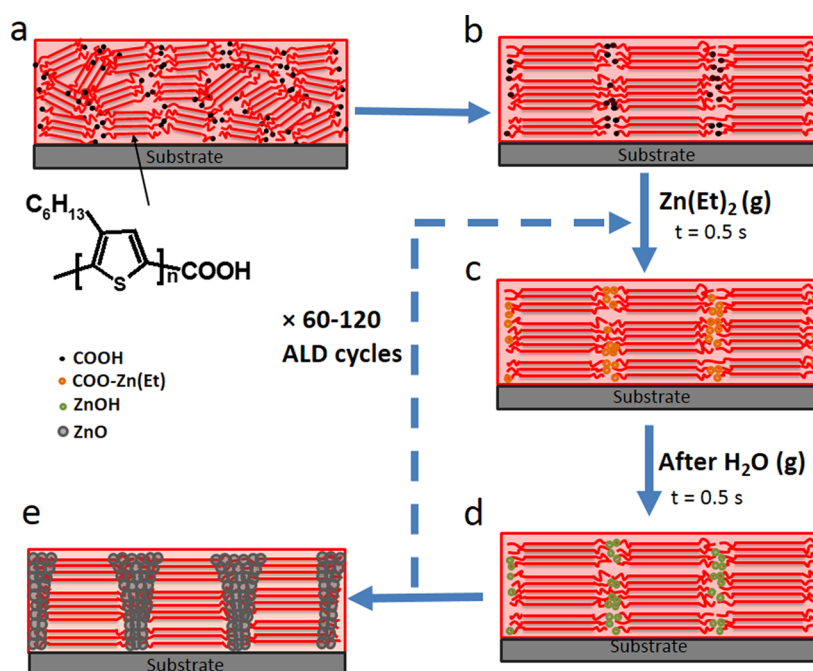


Figure 1. Schematic cross-sectional view of the processing steps: (a) Functionalized P3HT is spin-coated. (b) The film is annealed above its melting temperature and cooled down slowly to enhance crystallinity. The lower molecular weight of the P3HT allows the formation of well-ordered crystalline and amorphous domains. (c) After the ALD-like exposure to $\text{Zn}(\text{Et})_2$ and (d) to H_2O , ZnO is formed within the amorphous domains where the carboxylic acid end groups initiate the ZnO formation. (e) After several cycles (60–120) sheets of ZnO nanoclusters are formed within the polymer.

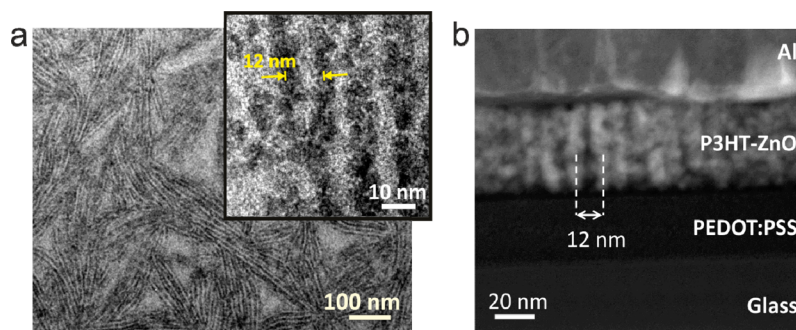


Figure 2. (a) Bright field transmission electron microscopy (TEM) image of the P3HT-ZnO film in plan-view. The inset shows the ZnO sheets consisting of nanoclusters. (b) The cross-sectional scanning transmission microscopy high-angle annular dark field image of the P3HT-ZnO structure shows that the ZnO lamellar structure spans the entire film.

allow high morphological control. However, pore filling and infiltration with an organic compound remains challenging.¹⁴ An alternative approach involves the in situ synthesis of ZnO nanoparticles from a diethylzinc–polymer solution. In the presence of a controlled humid atmosphere the Zn precursor is converted into ZnO. However, this process still suffers from a large variability in the domain sizes of both the P3HT and ZnO because of little control over the blend morphology and interfaces during P3HT crystallization.^{15,16}

We employ P3HT with low polydispersity that can self-organize into a periodic superstructure of amorphous and crystalline domains. The crystallinity and the ordering into this superstructure can be significantly increased by choosing the right annealing protocols which involve cooling the film from its melt with a defined cooling rate. Fully chain extended crystals, that is, chains without folding on top of each other, are usually formed with molecular weights below 20 kg/mol.¹⁸ The typical length scale of these periodic structures is determined by

the contour length of the polymer chain which is on the order of 10 nm. This is the same length scale which occurs in the phase separation of P3HT and fullerenes for example.¹⁹ To introduce the metal oxide into the amorphous domains of the superstructure (chain folds and chain ends adjacent to the crystalline region), we incorporated a simple carboxylic acid end group to the P3HT²⁰ which serves as a reactive site for the metal oxide growth. The accumulation of the acid groups in the amorphous interlayers is an important feature of this system as shown in Figure 1b.

The system investigated here does function as a bulk heterojunction photovoltaic device, with ZnO as the electron acceptor and P3HT as the donor. This is an attractive system due to its processability and low cost, as well as optoelectronic properties and elemental abundance of its constituent materials. ZnO easily crystallizes at temperatures above 80 °C, provides a high charge carrier mobility, and has a suitable work function.²¹ We note that the 10 nm length scale of the ZnO–P3HT

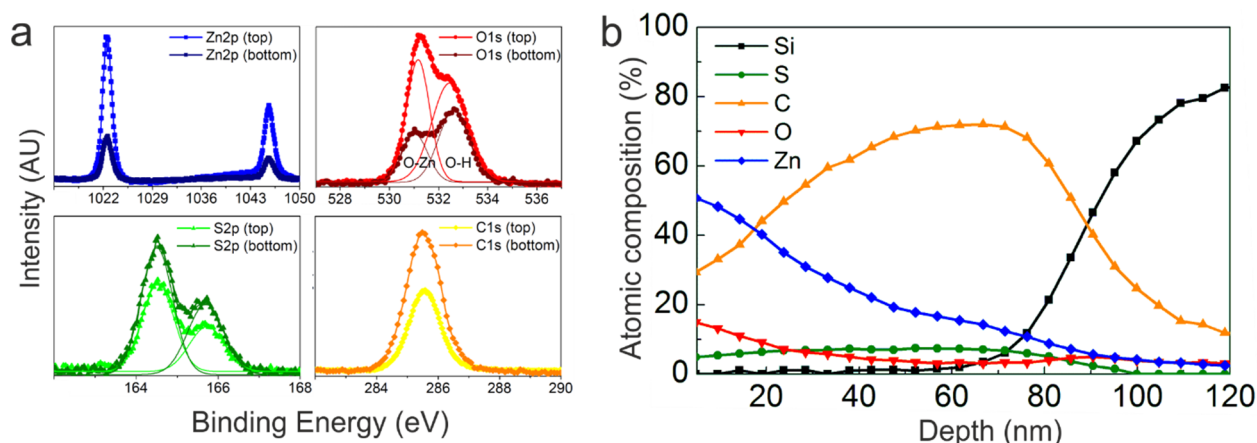


Figure 3. (a) Zn2p, O1s, S2p, and C1s XPS spectra of the top and bottom surfaces of a P3HT-ZnO (80 ALD-like cycles) film. (b) Atomic percentage XPS depth profile of a similar film on Si.

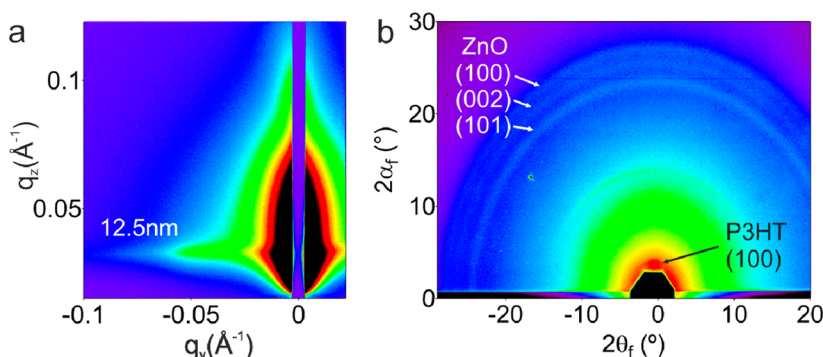


Figure 4. (a) GISAXS pattern of P3HT-ZnO and (b) corresponding GIWAXS, as a function of the scattering angle, showing functionalized P3HT and ZnO crystallinity. The arrows indicate the scattering peaks corresponding to the reflections arising from the crystalline structure of P3HT-COOH and the wurtzite structure of ZnO.

structures reported below matches the length scales required for excitonic photovoltaic devices.^{22–24}

To fabricate the hybrid P3HT-ZnO nanostructures, low molecular weight P3HT-COOH ($M_w = 5.6$ kg/mol) was spin-cast on top of poly(3,4-ethylenedioxythiophene)-poly(styrene sulfonate) (PEDOT:PSS) coated indium-tin oxide (ITO) substrates. The polymer film was heated up to 175 °C (above its melting point) and then gradually cooled (5 °C/min) to allow a slow recrystallization of the polymer and form a well-ordered superstructure of crystalline and amorphous domains, as shown in Figure 1. The polymer film was then introduced into an ALD chamber where it was sequentially exposed to diethylzinc and water under low pressure.²⁵ Diethylzinc ($\text{Zn}(\text{Et})_2$) diffuses into the amorphous domains and reacts with the carboxylic acid groups. The H_2O pulse reacts with the surface-attached $\text{Zn}(\text{Et})$ to form Zn-OH , releasing ethane. Periodic cycling of $\text{Zn}(\text{Et})_2$ and H_2O builds up ZnO in a sequential fashion as shown in Figure 1c–e.

Transmission electron microscopy (TEM) images of the resulting P3HT-ZnO hybrid film (after 60 cycles at 80 °C) are shown in Figure 2a. In plan-view TEM, we observe the formation of long (200–500 nm) sheets of ZnO nanoclusters with a mean size of 3.7 ± 0.9 nm (Figure 2a). The separation between sheets is 12.3 ± 1.6 nm, which agrees with the contour length of a fully extended P3HT polymer chain of 5.6 kg/mol molecular weight. This suggests that ZnO nanoclusters form within the semicrystalline P3HT structure in the amorphous regions of the polymer. Cross-sectional images give further

insight into the 3D arrangement of ZnO within the polymer film (Figure 2b). The ZnO nanoclusters penetrate the full depth of the 50 nm polymer film and organize into sheets spaced 12 nm apart.

The film composition was characterized by X-ray photoelectron spectroscopy (XPS). XPS spectra (Zn2p, O1s, S2p, and C1s signals) were collected on the top and bottom of a 90 nm hybrid film (80 ALD-like cycles at 80 °C, Figure 3a). The top surface of the film revealed a Zn composition of more than 50%. The Zn2p doublet appears at energies of 1022.5 and 1045.6 eV, consistent with previous measurements on ZnO deposited by ALD²⁶ or other techniques.²¹ The O1s spectrum revealed two species at 531 and 532.4 eV, which are attributed to O-Zn and hydroxide (O-H) oxygen atoms, respectively. The depth distribution of ZnO nanoclusters into the polymer film was determined by XPS depth profiling (Figure 3b). We observe a decay in the Zn signal with distance from 50% at the top surface to 6–7% at the bottom interface of the 90 nm film. This is in agreement with the XPS measurements on the bottom surface of films floated-off the substrate in deionized water. The decay of the Zn signal suggests that ZnO formation in amorphous P3HT is limited either by Fickian diffusion or by a reaction-diffusion process of diethylzinc (diethylzinc reacting with COOH or preformed ZnOH). A rough estimate taking into account the total exposure time to the precursor and neglecting its reaction with the sample gives a diffusion coefficient of diethylzinc in amorphous P3HT-COOH on the order of $10^{-13} \text{ cm}^2 \text{ s}^{-1}$.

Grazing incidence small angle and wide-angle X-ray scattering (GISAXS/GIWAXS) were performed to further investigate the structure of the hybrid composite. Figure 4a shows the GISAXS pattern of the P3HT–ZnO film (60 ALD-like cycles, 80 °C), which indicates a structural periodicity of 12.5 nm, in agreement with the results discussed above. The corresponding GIWAXS (Figure 4b) image shows the crystalline features of both P3HT and ZnO. The ZnO scattering pattern is relatively faint because of the low ZnO loading in the film. This signal nonetheless shows the existence of crystalline ZnO and can be assigned to the wurtzite structure of ZnO.²⁷ As shown in the Supporting Information, the ZnO crystallinity can be further enhanced at higher deposition temperatures (Figure S1).

The crystallinity of P3HT and the take-up of ZnO are also evident in optical absorption. Figure 5 shows the absorption

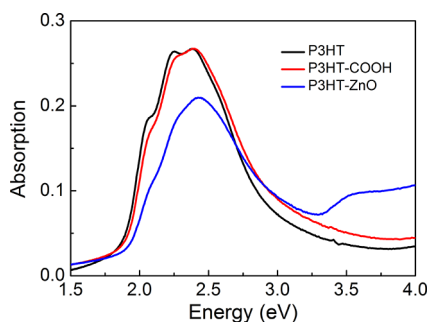


Figure 5. UV–vis absorption spectra of pure P3HT (black), functionalized P3HT–COOH (red), and P3HT–ZnO (blue) films.

spectra of a P3HT–ZnO film and compares it to films of pure P3HT and functionalized P3HT–COOH of similar molecular weight. The P3HT absorption spectra are a superposition of contributions from crystalline and amorphous fractions. According to the weakly coupled H-aggregates model,^{28,29} crystalline P3HT has distinct vibronic features above 2.08 eV, spaced at 0.18 eV intervals. The ratio of the 0–0 (2.08 eV) and 0–1 (2.26 eV) vibronic transitions is related to the order and crystallinity of P3HT. In contrast, amorphous P3HT shows a broad absorption feature at 2.5 eV with a lower absorption coefficient. Figure 5 shows that the 0–0/0–1 peak ratio decreases slightly with the inclusion of the COOH group as observed previously.²⁰ After ZnO processing a further decrease is observable which indicates a further reduction in the ordering of P3HT. Increased scattering may contribute to the overall decrease. Additionally, at the same time the feature for amorphous P3HT centered at 2.5 eV broadens, and ZnO absorption starting from 3.3 eV becomes evident. The decrease in P3HT crystallinity upon ZnO precursor exposure arises either from the mechanical disturbance of the polymer by the ZnO growth and crystallization or by the gradual dissolution of the P3HT crystalline lamellae by the $\text{Zn}(\text{Et})_2$ precursor, which starts by swelling the amorphous regions and then spreads into the crystalline regions. Comparing the film thicknesses before and after ZnO processing reveal an increase of film thickness up to 30–50%, depending on the initial films thickness and cycle times (see Supporting Information, S2).

A unique advantage of our deposition method is that the P3HT crystalline domains remain electronically functional as a photoactive material. The insertion of ZnO therefore produces a heterojunction for photovoltaic devices, as shown in the inset

of Figure 6a. The relative amount of ZnO within the film can be controlled by the duration or the number of deposition cycles.

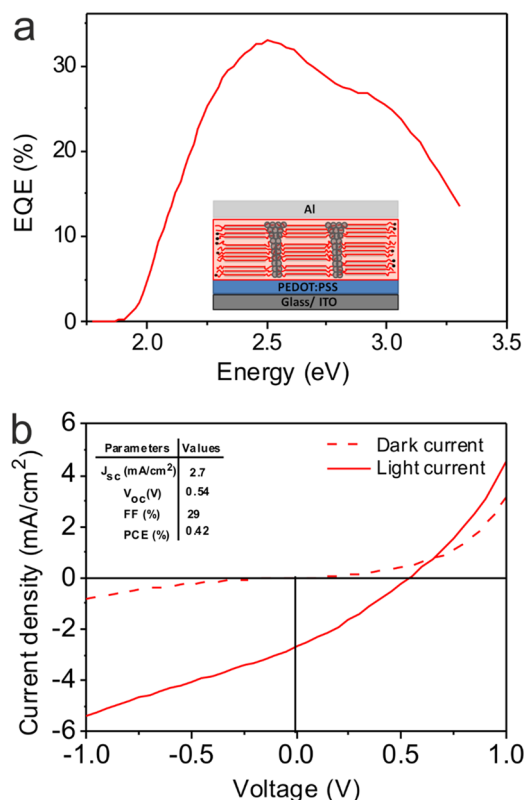


Figure 6. (a) External quantum efficiency (EQE) measurements for a device with a 30 nm P3HT film. A schematic diagram of the device architecture is shown in the inset. (b) Dark (dashed) and illuminated (solid) J – V curves for the same device. Photovoltaic device parameters are summarized in the inset.

Figure 5a shows the external quantum efficiency (EQE) measurement of a device with a 30 nm P3HT film. The EQE reaches a maximum value of 33%, which is higher than previously reported for unmodified P3HT–ZnO nanocrystal blends,³⁰ P3HT–ZnO nanorods,³¹ or in situ grown ZnO–P3HT blends.³² Taking into account the absorption, an internal quantum efficiency (IQE) of 55% can be estimated (the highest reported so far for P3HT–ZnO). Figure 6b shows the J – V characteristics in the dark and under AM1.5 illumination, with the photovoltaic performance parameters summarized in the inset. The open-circuit voltage (V_{oc}) was measured to be 0.54 V and up to 0.7 V when thicker P3HT films layer were used (90 nm).

In conclusion, we have demonstrated that the natural length scale for the interlamellar spacing in a semicrystalline polymer can be used to direct sub-10 nm growth of a two-component heterostructure. We have used P3HT both because it is itself a functional, semiconducting polymer and because it does form a suitable crystalline ordered structure. We consider that this method is fully general, can be extended to other polymers and to other inorganic counterparts, and therefore provides a very promising means for controlling nanostructure length scales in such composite materials.

P3HT–COOH carrying precisely one COOH group was synthesized using controlled Kumada catalyst transfer polymerization and further end group modification.²⁰ The molecular

weight of the here used sample is $M_w = 5.6$ kg/mol ($M_n = 4.9$ kg/mol) with a polydispersity of 1.16. P3HT with a similar molecular weight, regioregularity, and polydispersity is used as a reference material. Diethylzinc (Zn, 52 wt %) was purchased from Sigma-Aldrich.

Quartz glass, ITO-coated glass, and silicon substrates were used for UV-vis, electrical, and X-ray measurements, respectively. The substrates were first cleaned in an ultrasonic bath for 10 min in acetone and isopropanol followed by plasma etching for 10 min. A PEDOT:PSS layer was spin-cast on the ITO-glass substrates, annealed at 160 °C for 40 min, and then cooled down over 10 min. P3HT-COOH films were spin-cast from 5 mg/ml to 25 mg/ml chloroform solutions in a nitrogen-filled glovebox at 2000 rpm resulting in 30 to 160 nm P3HT film, respectively. For XPS measurements, P3HT was spin-coated on conductive silicon substrates. The samples were then heated to 175 °C (above the P3HT melting point) and cooled down to ambient temperature at a rate of 5 °C/min. These films were introduced into a Beneq ALD system and sequentially exposed to diethylzinc and water using a 0.5 s pulse time and 2 s purge time for both at 80 °C. Each sequence of diethylzinc and water exposure formed one cycle. The number of deposited cycles was varied between 60 and 120.

Transmission electron microscopy (TEM) was performed on a FEI Tecnai F20 microscope operated at 200 kV. The preparation of cross-sectional lamellar specimens was carried out on a FEI Helios dual beam FEG SEM/FIB microscope, equipped with an Omniprobe micromanipulator for in situ lift-out. High-angle annular dark field images of cross-sectional specimens were acquired using a Fischione detector on the FEI Tecnai F20 microscope, operated at 200 kV in scanning TEM (STEM) mode. See the Supporting Information (S3, S4) for the statistical analysis of size and spacing of the nanocluster sheets.

The photoemission spectroscopy samples were transferred into an ultrahigh vacuum chamber (ESCALAB 250Xi) for XPS measurements and depth profiling. XPS measurements were carried out using a XR6 monochromated Al K α X-ray source ($h\nu = 1486.6$ eV) with a 650 μ m spot size. An Ar⁺ ion gun with ion energy of 3000 eV was used for etching in depth profiling mode.

Grazing incidence small- and wide-angle X-ray scattering (GISAXS/GIWAXS) were performed at beamline D1, at the Cornell High Energy Synchrotron Source (CHESS) at Cornell University in Ithaca, NY, U.S.A. The wavelength was 1.17 Å. The beam was focused to a size of 500 μ m \times 100 μ m (horizontal \times vertical) at the sample position. A beam stop for the primary beam and the small-angle X-ray scattering signal was employed. A CCD detector with a pixel size of 46.9 μ m \times 46.9 μ m was used for GISAXS with a sample-detector distance of 1.846 m. To choose the appropriate incident angle, an X-ray reflectometry scan was performed before recording the image. GISAXS images were then taken at an incident angle (α_i) of 0.14°, which is slightly higher than the critical angle of the polymer film (α_{cp}). The measuring time was 1 s. For GIWAXS measurements, a Fujifilm image plate together with a GE Typhoon FLA 7000 developer was used allowing an area of 2500 \times 2000 pixels. The exposure time was 90 s, and the sample-detector distance was 0.25 m at an incident angle of 0.4°. The samples were moved out of the beam after each measurement to avoid beam damage.

UV-vis absorption was measured using a Hewlett-Packard 8453 UV-vis spectrometer with a 280–1100 nm spectral

range. Respective photoluminescence spectra can be found in the Supporting Information (S5).

Solar cells were fabricated by capping the composite films with 100 nm of aluminum as a top contact (cathode) and encapsulating them in a glovebox. External quantum efficiencies (EQE) were measured in air with a 250 W tungsten halogen lamp and an Oriel Cornerstone 130 monochromator as a function of wavelength at intensities less than 1 mW/cm². Current density versus voltage (J - V) curves were measured under AM 1.5 illumination with an ABET Solar 2000 solar simulator. The spectral mismatch factor determined with a calibrated inorganic solar cell under AM 1.5 conditions was considered in the efficiency calculation. The characterization for 90 nm P3HT film is reported in the Supporting Information (S6).

■ ASSOCIATED CONTENT

Supporting Information

S1, GIWAXS and GISAXS for films and ZnO prepared at different temperatures; S2, UV-vis and thickness change before and after ZnO processing for different initial film thicknesses; S3, ZnO particle diameter distribution; S4, spacing between ZnO sheets; S5, PL quenching for P3HT-ZnO film; S6, J - V curve and EQE for thicker film thicknesses. This material is available free of charge via the Internet at <http://pubs.acs.org>.

■ AUTHOR INFORMATION

Corresponding Author

*E-mail: rhf10@cam.ac.uk.

Notes

The authors declare no competing financial interest.

■ ACKNOWLEDGMENTS

We like to thank Zhi Kuang Tan and Pedro Cunha for helpful discussions. R.S.M. acknowledges the Marie-Curie superior network and S.H. and R.H.F. the EPSRC (UK) for funding. M.T. and R.L. acknowledge the financial support by the DFG (SFB 840). K.P.M. acknowledges Girton College (Cambridge) for funding. Part of this work is based upon research conducted at beamline D1 at the Cornell High Energy Synchrotron Source (CHESS). We thank U. Wiesner for fruitful discussions. We thank D.-M. Smilgies, J. Werner, and H. Sai for their help during the D1 experiment at CHESS.

■ REFERENCES

- (1) Sofos, M.; Goldberger, J.; Stone, D. A.; Allen, J. E.; Ma, Q.; Herman, D. J.; Tsai, W.; Lauhon, L. J.; Stupp, S. I. *Nat. Mater.* **2009**, *8*, 68–75.
- (2) Zhang, Q.; Atay, T.; Tischler, J. R.; Bradley, M. S.; Bulović, V.; Nurmikko, A. V. *Nat. Nanotechnol.* **2007**, *2*, 555–559.
- (3) Vendamme, R.; Onoue, S.; Nakao, A.; Kunitake, T. *Nat. Mater.* **2006**, *5*, 494–501.
- (4) Jiang, C.; Markutsya, S.; Pikus, Y.; Tsukruk, V. V. *Nat. Mater.* **2004**, *3*, 721–728.
- (5) Romero, P. G.; Chojak, M.; Cuentas-Gallegos, K.; Asensio, J. A.; Kulesza, P. J.; Casañ-Pastor, N.; Lira-Cantú, M. *Electrochem. Commun.* **2003**, *5*, 149–153.
- (6) Shim, H. W.; Jin, Y.; Seo, S.; Lee, S.; Kim, D. *ACS Nano* **2011**, *5*, 443–449.
- (7) Law, M.; Greene, L.; Johnson, J. C.; Saykally, R.; Yang, P. *Nat. Mater.* **2005**, *4*, 455–459.
- (8) Wang, X.; Wang, X.; Kim, K.; Wang, Y.; Stadermann, M.; Noy, M.; Hamza, A. V.; Yang, J.; Sirbully, D. J. *Nano Lett.* **2010**, *10*, 4901–4907.

- (9) Schmidt-Mende, L.; MacManus-Driscoll, J. L. *Mater. Today* **2007**, *10*, 40–48.
- (10) Xu, S.; Zhong, L. W. *Nano Res.* **2011**, *4*, 1013–1098.
- (11) Beek, W. J. E.; Wienk, M. M.; Janssen, R. A. J. *Adv. Mater.* **2004**, *16*, 1009–1013.
- (12) Boucle, J.; Ravirajan, P.; Nelson, J. J. *Mater. Chem.* **2007**, *17*, 3141–3153.
- (13) Greene, L. E.; Law, M.; Yuhas, B. D.; Yang, P. *J. Phys. Chem. C* **2007**, *111*, 18451–18456.
- (14) Ravirajan, P.; Ravirajan, P.; Peiró, A. M.; Nazeeruddin, M. K.; Graetzel, M.; Bradley, D. D. C.; Durrant, J. R.; Nelson, J. J. *J. Phys. Chem. B* **2006**, *110*, 7635–7639.
- (15) Oosterhout, S. D.; Wienk, M. M.; van Bavel, S. S.; Thiedmann, R.; Koster, L. J. A.; Gilot, J.; Loos, J.; Schmidt, V.; Janssen, R. J. A. *Nat. Mater.* **2009**, *8*, 818–824.
- (16) Oosterhout, S. D.; Koster, L. J. A.; van Bavel, S. S.; Loos, J.; Stenzel, O.; Thiedmann, R.; Schmidt, V.; Campo, B.; Cleij, T. J.; Lutzen, L.; Vanderzande, D.; Wienk, M. M.; Janssen, R. J. A. *Adv. Energy Mater.* **2011**, *1*, 90–96.
- (17) Moet, D. J. D.; Koster, L. J. A.; de Boer, B.; Blom, P. W. M. *Chem. Mater.* **2007**, *19*, 5856–5861.
- (18) Wu, Z.; Petzold, A.; Henze, T.; Thurn-Albrecht, T.; Lohwasser, R. H.; Sommer, M.; Thelakkat, M. *Macromolecules* **2010**, *43*, 4646–4653.
- (19) Kohn, P.; Rong, Z.; Scherer, K. H.; Sepe, A.; Sommer, M.; Müller-Buschbaum, P.; Friend, R. H.; Steiner, U.; Hüttner, S. *Macromolecules* **2013**, *46*, 4002–4013.
- (20) Lohwasser, R. H.; Thelakkat, M. *Macromolecules* **2010**, *43*, 7611–7616.
- (21) Vaynzof, Y.; Kabra, D.; Zhao, L.; Ho, P. K. H.; Wee, A. T. S.; Friend, R. H. F. *Appl. Phys. Lett.* **2010**, *97*, 033309–033309-3.
- (22) Kohn, P.; Huettner, S.; Komber, H.; Senkovskyy, V.; Tkachov, R.; Kiriya, A.; Friend, R. H.; Steiner, U.; Huck, W. T. S.; Sommer, J.; Sommer, M. *J. Am. Chem. Soc.* **2012**, *134*, 4790–4805.
- (23) Brinkmann, M.; Rannou, P. *Adv. Funct. Mater.* **2007**, *17*, 101–108.
- (24) Brinkmann, M.; Rannou, P. *Macromolecules* **2009**, *42*, 1125–1130.
- (25) Guziewicz, E.; Godlewski, M.; Krajewski, T.; Wachnicki, Ł.; Szczepanik, A.; Kopalko, K.; Wójcik-Głodowska, A.; Przeździecka, E.; Paszkowicz, W.; Łusakowska, E.; Kruszewski, P.; Huby, N.; Tallarida, G.; Ferrari, S. J. *Appl. Phys.* **2009**, *105*, 122413.
- (26) Ehrler, B.; Musselman, K. P.; Böhm, M. L.; Morgenstern, F. S. F.; Vaynzof, Y.; Walker, B. J.; MacManus-Driscoll, J. L.; Greenham, N. C. *ACS Nano* **2013**, *7*, 4210–4220.
- (27) Wagata, H.; Ohashi, N.; Taniguchi, T.; Katsumata, K.; Okada, K.; Matsushita, N. *Cryst. Growth Des.* **2010**, *10*, 4968–4975.
- (28) Clark, J.; Silva, C.; Friend, R. H.; Spano, F. C. *Phys. Rev. Lett.* **2007**, *98*, 206406–206406.
- (29) Clark, J.; Chang, J. F.; Spano, F. C.; Friend, R. H.; Silva, C. *Appl. Phys. Lett.* **2009**, *94*, 163306–163306-3.
- (30) Li, F.; Chen, W.; Yuan, K.; Chen, Y. *Org. Electron.* **2012**, *13*, 2757–2762.
- (31) Olson, D. C.; Shaheen, S. E.; Collins, R. T.; Ginley, D. S. *J. Phys. Chem.* **2007**, *111*, 16670–16678.
- (32) Beek, W. J. E.; Wienk, M. M.; Janssen, R. A. J. *Adv. Funct. Mater.* **2006**, *16*, 1112–1116.